https://doi.org/10.1038/s44182-026-00106-y

Insect-inspired hexapod robot with magnetically coupled compliant and modular drive system

Check for updates

Donato Romano [1,2] ✉ & Gianluca Manduca [1,2]

Legged robots are increasingly inspired by insects' ability to combine rigidity and compliance for agile, damage-tolerant locomotion in cluttered terrain. Herein, we introduce INSECTRON, a centimeter-scale hexapod robot that employs magnetic transmission to achieve robust mobility with minimal mechanical complexity. Each leg connects to the drivetrain via neodymium magnets, forming a self-aligning micro-clutch that transmits torque under normal load and safely slips under overload, while additional magnetic couplings between drive modules accommodate load imbalances and perturbations. Hall effect sensors provide proprioception for a phase-domain controller maintaining persistent anti-phase coordination. The magnetic transmission architecture introduces intrinsic mechanical adaptability, functionally analogous to biological preflex mechanisms, enabling rapid responses to external perturbations without additional control complexity. Experiments demonstrated stable locomotion across multiple slopes and substrates. Maneuverability was achieved through differential turning and spin-in-place. A minimum Cost of Transport (CoT) of 30 was achieved during locomotion experiments. Under vertical perturbations, INSECTRON autonomously recovered in over 90% of trials, highlighting strong passive impact tolerance. The architecture eliminates the need for precision alignment and mechanical fasteners, enabling tool-free leg replacement and rapid mechanical reconfiguration. This work establishes a scalable route toward modular, resilient, and field-deployable miniature legged robots for confined and uncertain environments.

Legged robotics has long been inspired by nature's most dynamic and adaptive biological models (e.g. mammals, birds, arthropods, etc.)[1–3]. These animals have remarkable locomotion capabilities, swiftly moving through cluttered landscapes, climbing vertical surfaces, and squeezing through tight crevices[4,5]. Animals achieve such feats through a combination of mechanical redundancy, distributed control, and structural compliance. While biological systems naturally combine compliance and robustness, achieving similar properties in compact robotic mechanisms remains challenging. In particular, small legged robots often rely on rigid transmissions that are vulnerable to shocks, overload, and leg entanglement. Among bio-inspired legged robotic platforms, hexapod robots, featured by their six-legged structure, represent a particularly effective approach to navigate unstructured and uneven terrains[6,7]. Their multi-legged configuration provides high stability, fault tolerance, and redundancy, making them suitable for challenging environments where wheeled or tracked robots struggle. Hexapod robots have promising applications in search and rescue missions, planetary exploration, disaster response, and industrial inspection, where mobility over complex, unpredictable terrain is critical[7,8].

Traditional legged robots generally exploit rigid mechanical joints, fixed fasteners, and precisely aligned shafts to transmit motion from motors to leg assemblies[9]. While effective, these conventional approaches impose limitations in terms of modularity, complexity, and long-term wear. Replacing or servicing a damaged leg can be time-consuming and invasive, often requiring the disassembly of surrounding components. Moreover, rigid mechanical linkages can be vulnerable to shock loads and misalignment, especially in dynamic environments.

Despite the progress achieved in legged robotics, a key challenge remains in designing locomotion mechanisms that combine compact actuation, mechanical robustness, and tolerance to unexpected disturbances while maintaining system simplicity. In particular, small-scale legged robots are especially vulnerable to impacts, terrain irregularities, and leg entanglement, which can generate excessive loads on rigid transmissions and lead to mechanical failure or motor stall. This raises a fundamental question:

[1]The BioRobotics Institute, Sant'Anna School of Advanced Studies, Pisa, Italy. [2]Department of Excellence in Robotics and AI, Sant'Anna School of Advanced Studies, Pisa, Italy. ✉e-mail: donato.romano@santannapisa.it

Can legged locomotion mechanisms be designed to passively tolerate overloads and recover from disturbances while preserving compact and efficient actuation architectures? Addressing this question requires exploring alternative transmission concepts that introduce compliance and self-protection directly within the drivetrain without relying on complex sensing or control strategies.

Herein, we present INSECTRON, a hexapod robot with a novel approach to mechanical coupling between the drive system and the legs. Inspired by the many insects' remarkable ability to navigate confined, cluttered, and dynamic terrains through a combination of rigid and highly compliant body structures[10,11], our design is based on a bioinspired, mechanically compliant interface. Each leg is attached to the robot's internal gear-driven system via magnetic coupling, a non-rigid connection that replaces traditional mechanical fasteners such as pins or bolts. The robot's core structure consists of six legs organized into two drive modules. Each module is actuated by a DC micromotor through a compact gear transmission, with three legs mechanically synchronized on each side. Motion is transmitted from the motor to the output gears, which are magnetically coupled to the leg mechanisms, generating coordinated leg oscillations during locomotion. Careful alignment of magnetic poles maximizes torque transfer while minimizing slippage. Additionally, the two halves of the robot on either side of the sagittal plane are also magnetically coupled, allowing controlled flexion across the midline and emulating insects' ability (e.g. cockroaches) to modulate body stiffness and shape during confined locomotion.

Beyond morphological inspiration, arthropod locomotion relies on distributed neuromechanical control that enables rapid responses to environmental perturbations. Load-sensitive reflex pathways and local proprioceptive feedback modulate limb stiffness and force output during locomotion, enhancing robustness in unpredictable terrains. Analogously, the magnetic transmission architecture of the present platform introduces intrinsic mechanical responsiveness resembling biological preflexes, enabling passive adaptation to external disturbances prior to higher-level control. This design extends bioinspiration beyond morphology to embodied mechanical intelligence observed in arthropod locomotor systems[12].

Magnetic couplings have been previously explored in applications such as fluid pumps[13], sealed mechanical systems[14], where maintaining isolation between compartments is critical, and recently in magnetic transmission systems for body-caudal swimming locomotion[15,16]. However, their use in legged locomotion represents a novel application. In our case, the coupling is not used to transmit torque through a barrier, but rather to simplify and modularize the connection between gear and limb, enabling fast prototyping, experimentation, and servicing.

From a mechanical perspective, this architecture reduces part count and eliminates the need for precise alignment tolerances often required by pinned or keyed joints. It also allows for a more flexible layout, where slight angular or radial misalignments between the gear and leg do not lead to binding or mechanical stress. The inherent compliance of the magnetic joint acts as a passive safety mechanism, absorbing minor impacts and preventing transmission of excessive forces to the internal drivetrain.

However, the use of magnetic coupling also introduces unique design challenges. Ensuring sufficient torque transmission without slippage requires careful calibration of magnet strength, spacing, and alignment[17,18]. In dynamic walking scenarios, inertial forces, friction, and uneven loading can lead to moments where magnetic torque is challenged. Nevertheless, the selected magnetic configuration provides reliable force transmission during nominal operation while preserving passive disengagement under overload conditions.

The walking gait of the robot are generated by two DC motors, whose rotation is transmitted to all the gears that are magnetically connected to the legs. Each gear-magnet-leg assembly receives synchronized motion from the motor, ensuring that every leg follows the same drive signal without the need for independent motor commands. Here a proprioceptive, phase-based control strategy is proposed that maintains the two drive modules in persistent anti-phase (180°).

Structurally, the robot's chassis remains compact and symmetric, with each leg mount evenly spaced to guarantee balance and uniform weight distribution across the platform. This configuration results in a lightweight yet robust system that effectively includes mechanical simplicity with functional adaptability. In this work, we experimentally evaluate the robot's locomotion performance in terms of forward speed, turning capability, and energetic consumption. We further assess robustness by testing locomotion across inclined surfaces. Different substrate types were also evaluated. Controlled perturbation and recovery experiments were performed to quantify the system's ability to withstand disturbances. Initial tests demonstrated that the magnetic coupling system maintained secure connections under normal loads while safely disengaging when overloaded, precisely as designed.

In summary, this study introduces a hexapod robot platform with a magnetically mediated drivetrain architecture for legged locomotion. The proposed design integrates (1) a compact gear-driven transmission capable of actuating multiple legs with minimal mechanical complexity, (2) magnetic micro-clutches at the gear-leg interface that provide passive overload protection, (3) magnetic clutches connecting the two drive modules to absorb transient load imbalances and impacts, and (4) a proper phase control strategy of the drive modules with contactless magnet-Hall sensing. This hybrid mechanical-magnetic design preserves the reliability of traditional geared drive systems while introducing a novel, highly modular method for linking the legs to the drivetrain. The platform enables streamlined assembly, maintainance, and modification, as well as features built-in shock tolerance and overload protection. By merging classical mechanical design with innovative coupling strategies, this work offers a practical and scalable solution to current challenges in legged robotics. It advances in modular robotics development, rapid prototyping, and the creation of resilient locomotion systems for field applications.

Results

Robot architecture and magnetic coupling system

This work presents a miniaturized hexapod robot, with a body length of 8.7 cm, that combines magnet-based mechanics with fully onboard electronics to achieve robust and controllable locomotion at small scale. The proposed architecture integrates a compact drivetrain with passive magnetic elements that simultaneously provide overload protection, mechanical robustness, and sensing.

Figure 1 illustrates the architecture and working principle of the locomotion mechanism, including exploded views of the drivetrain, the CAD representation of the transmission, and the fully assembled system. Locomotion is generated by two magnetically coupled, identical drive modules, with one rotated by 180° relative to the other, each powered by a DC micromotor. The rotational motion of each motor is reduced through a compact spur-gear train and converted into coordinated leg movement. In this configuration, three legs per side move with a defined phase. This design allows multiple legs to be actuated through a single compact transmission while maintaining coordinated motion across the drivetrain.

A key novelty of the platform lies in the use of magnet-based subsystems integrated directly into the drivetrain. The mechanical transmission incorporates magnetic couplings at the gear-leg interface that act as passive micro-clutches. When obstacles, terrain irregularities, or leg entanglement impose excessive torque on the drivetrain, the magnetic coupling temporarily disengages instead of rigidly stalling the motor. This passive compliance protects the gear train, prevents motor overcurrent, and enables automatic re-engagement once the disturbance is removed.

The two drive modules are mechanically connected through additional magnetic clutches. Under nominal operating conditions, this coupling synchronizes the two sides and distributes torque across the drivetrain. Unlike the gear-leg couplings, which primarily protect individual leg mechanisms, the magnetic clutches connecting the two drive modules accommodate transient load imbalances between the left and right modules. During impacts or asymmetric terrain interactions, controlled slip reduces

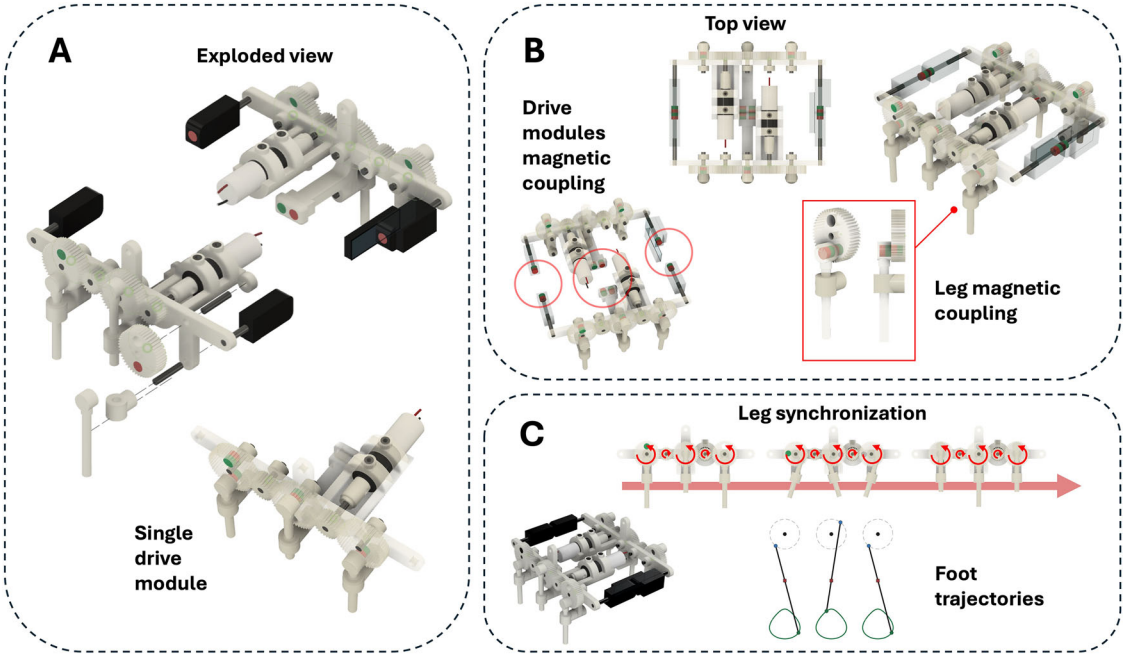


Fig. 1 | Mechanical architecture and operating principle of the proposed system. **A** Exploded view of the two drive modules. Each module integrates a DC micromotor, a spur-gear transmission, and three synchronized leg mechanisms. **B** Views of the complete robot architecture showing the two drive modules and the overall chassis layout. The inset highlights the magnetic coupling used to connect the two drive modules and the magnetic coupling between the rotating gear and the leg, enabling compliant torque transmission and passive disengagement under overload conditions. **C** Locomotion principle and leg synchronization. The three legs of each module are mechanically synchronized through the gear train and generate coordinated oscillatory motions during locomotion. The kinematic representation illustrates the phase relationship between the legs and the resulting periodic foot trajectories that produce alternating stance and swing phases.

the transmission of impulsive torsional loads across the robot while preserving overall locomotion performance.

Embedded magnet-Hall pairs mounted on selected gears provide contactless measurement of the output gear angular position on each side of the robot (see Fig. 2). The resulting signals provide proprioceptive feedback while maintaining a compact and mechanically robust sensing architecture.

Control is implemented entirely through onboard electronics that independently regulate the two drive modules. A phase-based closed-loop controller exploits measurements from the Hall effect sensors to maintain the desired coordination between the two drive modules. The robot can achieve coordinated straight locomotion, differential turning, and spin-in-place. Supplementary Movie 1 provides an overview of the robot design and representative experimental demonstrations.

Straight locomotion performance and energetic efficiency on flat and inclined terrain

The initial experiments assessed the robot's straight-line locomotion on a neutral ground surface consisting of a gridded paper sheet used for spatial calibration. Fig. 3A shows representative time-lapse snapshots of the miniature robot during straight locomotion. Across the tested frequency range the robot exhibits a clear monotonic increase in forward speed (Fig. 3B). Speed rises from 1.8 cm/s (0.21 BL/s) at 1.5 Hz to 2.7 cm/s (0.31 BL/s) at 1.9 Hz, indicating that higher stepping frequencies translate directly into faster forward progression. The slope of the speed-frequency relationship remains approximately constant.

Electrical power consumption shows comparatively smaller variations across the same frequency range (Fig. 3C). Power decreases slightly from 0.44 W at 1.5 Hz to 0.33 W around 1.8 Hz, before increasing again to 0.40 W at 1.9 Hz. Energy per meter decreases steadily from 24 J/m at 1.5 Hz to 14 J/m at 1.9 Hz (Fig. 3D). The corresponding Cost of Transport (CoT) decreases from 72 to 42 across the tested frequency range and indicating improved locomotion efficiency at higher frequencies.

To evaluate locomotion performance under terrain inclination, additional experiments were conducted on three slopes (0°, 3°, and 5°) under the same actuation conditions, at the maximum tested frequency (Fig. 3E–G). Increasing slope produces a substantial reduction in forward speed. At 0° the robot reaches 2.7 cm/s, while speed decreases to 1.6 cm/s at 3° and 0.8 cm/s at 5° (Fig. 3E). Electrical power consumption remains nearly constant across the three conditions, varying only slightly between 0.39 W and 0.41 W (Fig. 3F). Energy per meter rises from 15 J/m on flat ground to 26 J/m at 3°, reaching 50 J/m at 5° (Fig. 3G). The corresponding CoT values increase accordingly, indicating that locomotion becomes progressively less energy efficient as terrain inclination increases.

These experiments show that locomotion performance on neutral ground scales predictably with drive frequency, while terrain inclination primarily affects energetic efficiency by reducing effective forward progression.

Maneuverability: differential steering and spin-in-place

Two strategies were investigated to achieve maneuverability: differential steering and spin-in-place. Differential steering was achieved by actuating the two drive modules at different frequencies, generating curved trajectories whose curvature depended on the frequency difference between the modules. Representative image sequences are reported in Fig. 4A.

The differential-drive steering performance is summarized in Fig. 4B. As the absolute frequency difference between the two drive modules increased, the robot exhibited progressively stronger turning behavior. The angular speed increased from 0.11 rad/s to 0.23 rad/s, while the turning radius decreased from 0.2 m to below 0.1 m. This inverse relationship confirms the expected differential-drive mechanism, whereby increasing the frequency difference between the two drive modules generates larger yaw moments and consequently tighter trajectories. The results also demonstrate that the steering response can be continuously modulated through the frequency difference between the two sides, providing predictable control over the turning kinematics. The corresponding electrical power consumption is reported in Fig. 4C. Power increased across the tested steering conditions, from ~0.40 W to 0.60 W.

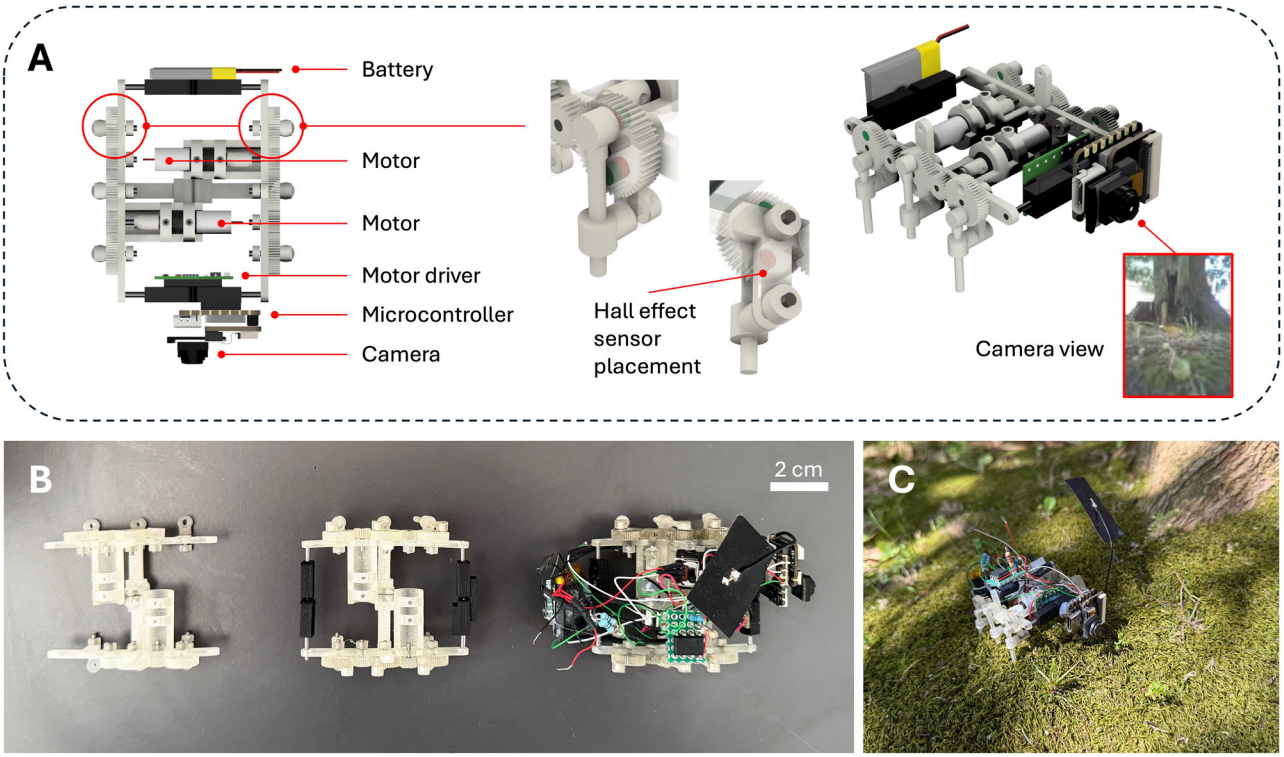


Fig. 2 | Hardware architecture and system integration of the robotic platform. **A** CAD views of the robot highlighting the integration of the main sensing, and electronic components. The labels identify the battery, dual DC micromotors, microcontroller, motor driver, and onboard camera. The red circles indicate the locations of the magnet-Hall sensing units used for indirect measurement of the output gear angular position on each drive module. Close-up views provide detailed illustrations of the Hall effect sensor placement. The inset image shows a representative frame acquired by the onboard camera during locomotion. **B** Fully assembled robot showing the compact integration of the locomotion mechanism, onboard electronics, wireless communication hardware, and vision system within the robot chassis. **C** Photograph of the fabricated prototype during outdoor locomotion experiments.

Spin-in-place was evaluated separately by driving the two modules at the same frequency in opposite directions, producing rotation about the body center. The maneuver was generated using the proposed phase-based control strategy. Representative image sequences are shown in Fig. 4D. The angular speed increased monotonically with drive frequency, rising from 0.71 rad/s at 1.5 Hz to nearly 0.90 rad/s at 1.9 Hz (Fig. 4E), demonstrating a direct relationship between motor cycling frequency and rotational performance.

The electrical power consumption during spin-in-place increased gradually with frequency, ranging from approximately 0.31 W to 0.37 W (Fig. 4F). When the energetic cost was normalized by the achieved angular displacement, the energy per radian remained relatively stable across the explored operating range (Fig. 4G). A minimum value of 0.37 J/rad was observed at intermediate frequencies, suggesting a trade-off between rotational speed and power consumption.

These results demonstrate that the platform provides controllable and repeatable maneuverability through two turning modalities. Differential steering enables continuous adjustment of trajectory curvature, whereas spin-in-place allows rapid reorientation around the body center. In both cases, substantial changes in rotational performance are achieved with relatively modest variations in power consumption.

Locomotion performance on different substrates

The locomotion performance of the robot was evaluated on four substrates: compact soil, sand, a coarse granular substrate composed of perlite particles, and field tests (grass). Representative image sequences in Fig. 5A illustrate the interaction between the robot and the different terrains during forward locomotion. In all conditions, the robot maintained a stable stepping pattern and continuous forward progression, demonstrating the ability to locomote on different surfaces.

The quantitative relationship between frequency and forward speed is reported in Fig. 5B. Across all tested substrates, locomotion speed increased with frequency, ranging from ~1.3–1.6 cm/s at the lowest frequencies to about 2.0 cm/s (0.23 BL/s) at the highest frequencies. Although the achievable speeds were broadly comparable across terrains, differences emerged in the frequencies attained under identical motor commands. The measured frequency provides an indirect indication of the effective load imposed by the substrate on the drivetrain. Lower frequencies therefore suggest increased terrain-dependent resistance, arising from differences in foot-ground interaction, substrate deformation, and slip. Despite these variations, the robot maintained stable forward locomotion on all tested surfaces.

The corresponding electrical power consumption is shown in Fig. 5C. Locomotion on granular perlite resulted in the highest power consumption, reaching approximately 0.60 W at the highest frequencies. In contrast, locomotion on sand and grass required less than 0.40 W, with the lowest power consumption measured on grass, remaining close to 0.20 W across most tested conditions. These results indicate that substrate properties strongly influence the mechanical load experienced by the drivetrain and, consequently, the energy required to sustain locomotion. The higher power demand observed on granular perlite is likely associated with increased energy dissipation caused by substrate deformation and reduced traction efficiency, whereas the lower consumption measured on grass suggests more favorable interaction conditions for locomotion.

Figure 5D highlights substantial differences in locomotion efficiency across the tested substrates. Locomotion on soil exhibited a progressive reduction in energy per meter with increasing frequency, decreasing from approximately 40 J/m to 20 J/m. In contrast, locomotion on sand remained relatively stable, with energy-per-meter values between 20 and 25 J/m across the explored frequency range. The highest energetic expenditure was

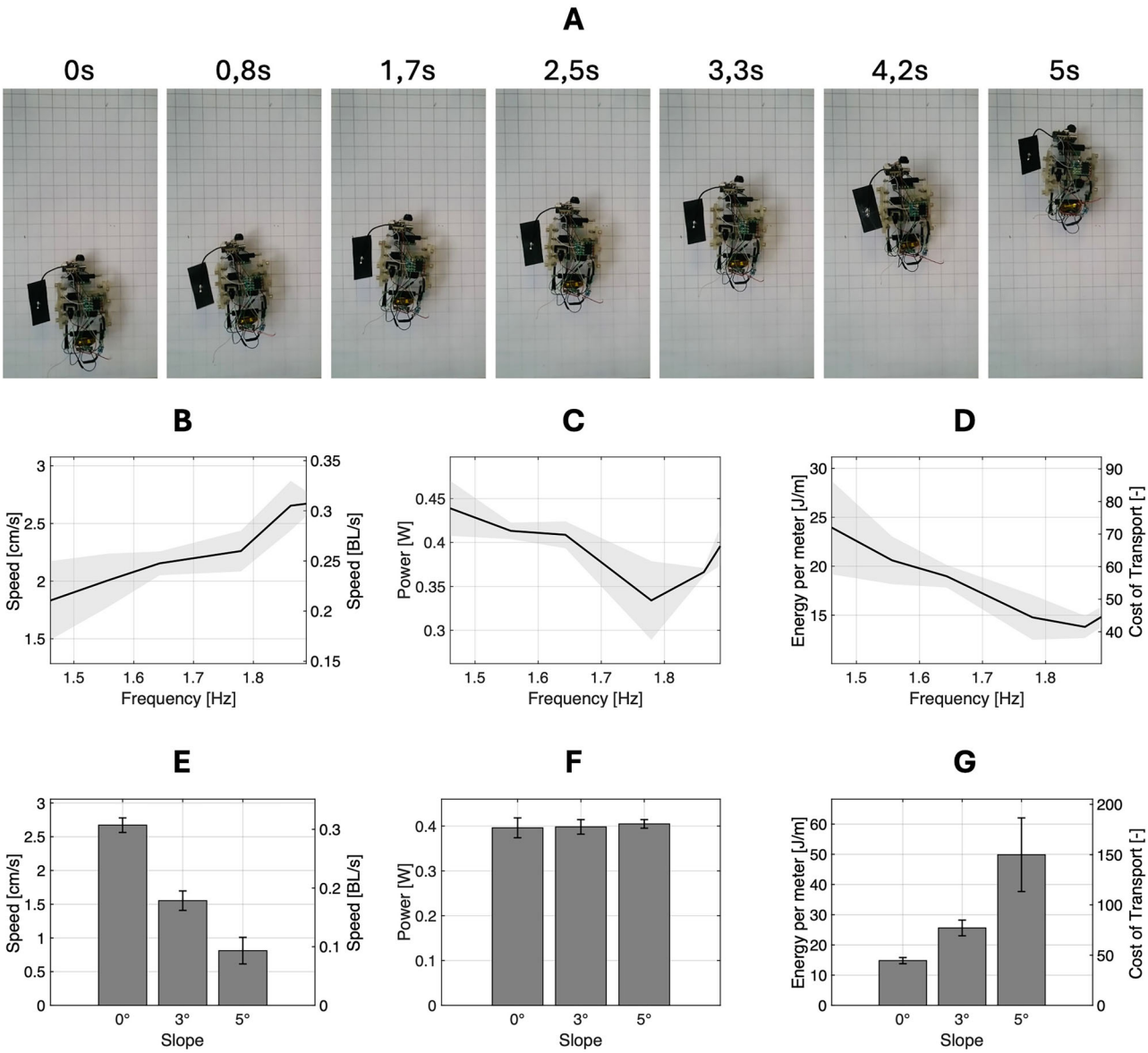


Fig. 3 | Locomotion performance on neutral ground and inclined terrain. **A** Representative time-lapse sequence of the robot performing straight locomotion on the neutral ground reference surface (gridded paper sheet), showing body progression over time. **B** Forward speed as a function of drive frequency on neutral ground. Solid lines represent mean values across replicates and shaded regions indicate standard deviation. **C** Electrical power consumption as a function of drive frequency on neutral ground. **D** Energy per meter and corresponding Cost of Transport (CoT) as functions of drive frequency. **E** Forward speed measured on three slopes (0°, 3°, and 5°) under the same actuation conditions (maximum tested frequency). Bars represent mean values and error bars indicate standard deviation. **F** Electrical power consumption across slopes. **G** Energy per meter and CoT across slopes.

measured during locomotion on granular perlite, where values approached 40 J/m, whereas the lowest energy-per-meter values were consistently observed on grass, remaining below 15 J/m over most tested conditions. Notably, the lowest locomotion cost across all tested substrates was achieved on grass, where the CoT reached a minimum value of 30. These results indicate that substrate properties have a strong influence on locomotion efficiency, affecting the energetic cost of transport even under conditions where comparable forward speeds are achieved.

These results demonstrate that the robot is capable of robust locomotion across compact, deformable, granular, and vegetated terrains. Although locomotion speed and energetic efficiency depend on substrate properties, the robot maintained stable operation in all tested conditions. This capability is particularly relevant for real-world deployments, where legged robotic systems are expected to encounter heterogeneous environments and continuously varying ground conditions.

Robustness to external perturbations

To evaluate the robustness of the platform under external perturbations, controlled vertical disturbances were applied to the robot body using a motorized linear actuator equipped with a rigid indenter. The indenter contacted the dorsal surface of the robot at two locations (P1 and P2), positioned above the drivetrain (Fig. 6A). The actuator applied repeatable vertical perturbations (Fig. 6B). The disturbance profile was defined by the duration for which the indenter remained in contact with the robot before being lifted. Three contact durations were tested: T1 = 0.1 s, T2 = 0.5 s, and T3 = 1 s. This protocol allowed us to evaluate the effect of different perturbation persistence times while keeping the applied disturbance configuration consistent.

A total of 360 trials were conducted, considering all timing conditions and both perturbation locations. After the indenter was lifted, the robot response was classified into three possible outcomes: successful recovery;

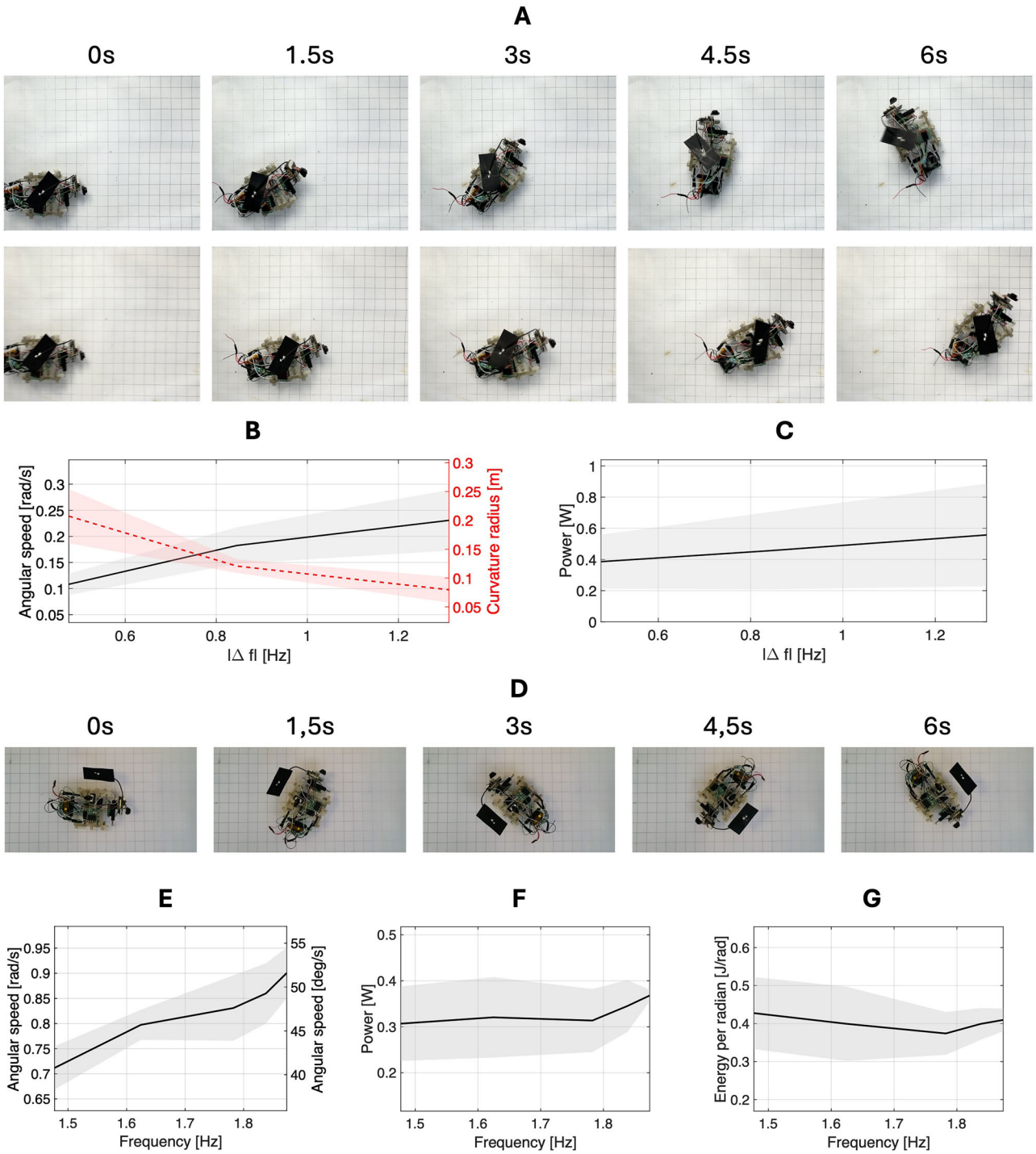


Fig. 4 | Characterization of turning behaviors. A Representative image sequence of differential steering obtained by actuating the two drive modules at different frequencies. The robot follows a curved trajectory whose curvature depends on the frequency difference between the two modules. **B** Angular speed and turning radius as a function of the absolute frequency difference between the two sides ($|\Delta f|$). Shaded areas indicate the standard deviation across trials. Both steering directions were evaluated. **C** Electrical power consumption during differential steering as a function of $|\Delta f|$. **D** Representative sequence of spin-in-place, obtained by driving the two sides at the same frequency in opposite directions while maintaining anti-phase coordination, producing rotation around the body center. **E** Angular speed as a function of drive frequency during spin-in-place experiments. Both steering directions were evaluated. **F** Electrical power consumption measured during spin-in-place. **G** Energy per radian versus drive frequency.

Failure 1, corresponding to an unstable or aborted recovery associated with legs; and Failure 2, corresponding to the inability of the two modules to immediately recover their nominal configuration after the perturbation.

Across all conditions the robot exhibited a high probability of successful recovery after the disturbance (Fig. 6C). The measured recovery probabilities were 0.91 for T1, 0.95 for T2, and 0.94 for T3, indicating that the platform regained stable configuration in most trials. The differences between timing conditions were relatively small, suggesting that the system maintains a high level of disturbance tolerance even when the perturbation persists for longer durations.

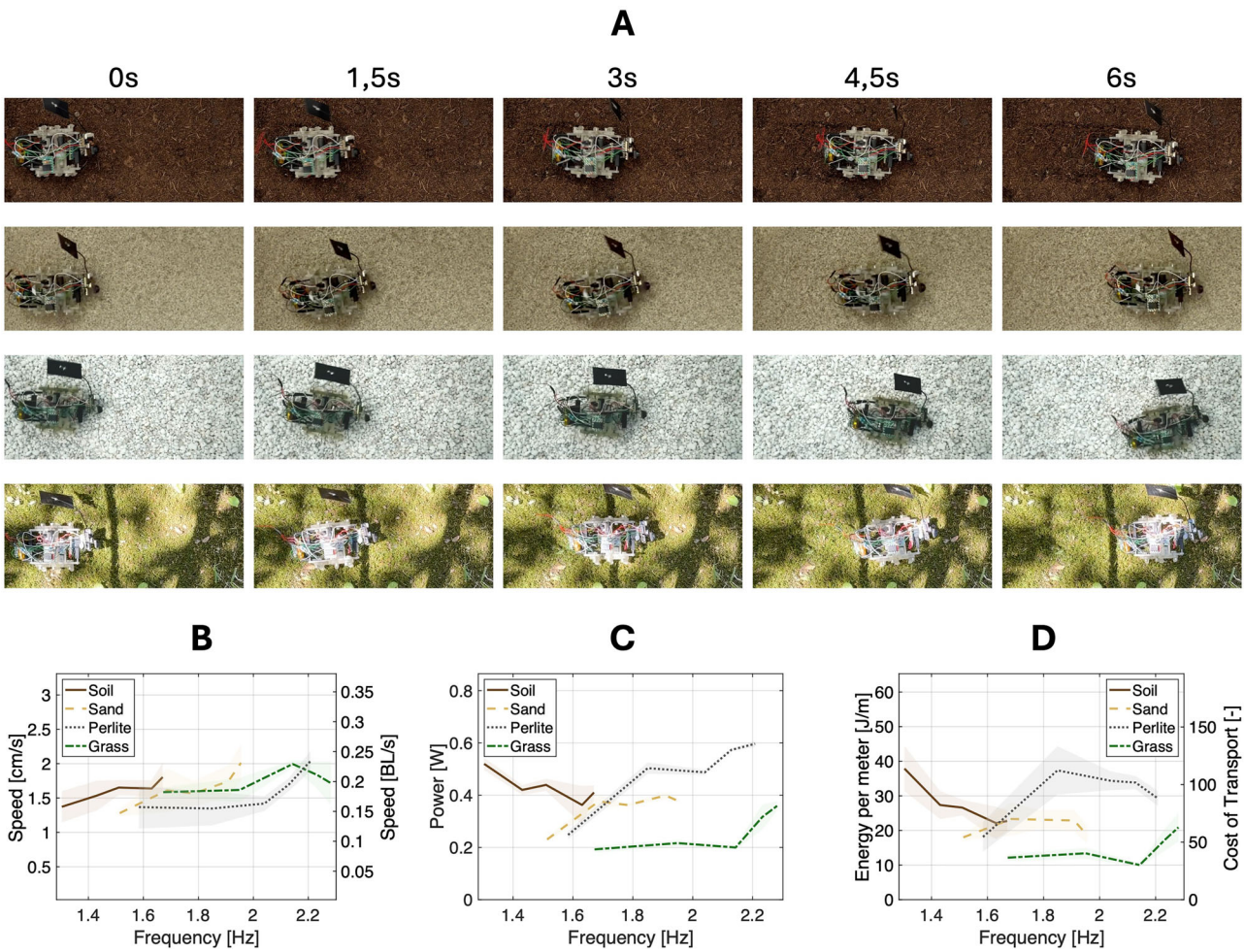


Fig. 5 | Locomotion performance across different substrates. A Representative time-lapse sequences of the robot performing straight locomotion on soil (first row), sand (second row), perlite (third row), and field/grass (fourth row). The snapshots illustrate the progression of the robot over time and its interaction with the different terrain conditions. **B** Forward speed as a function of drive frequency for the four substrates. The left axis reports speed in cm/s, while the right axis reports speed in body lengths per second (BL/s). **C** Electrical power consumption as a function of drive frequency. **D** Energy per meter (J/m) and corresponding Cost of Transport (CoT) as functions of drive frequency. Solid lines represent mean values across repeated trials, while shaded regions indicate standard deviation.

Failures were comparatively rare and were distributed between the two failure categories shown in Fig. 6D. Failure 1 accounted for probabilities of ~0.06, 0.06, and 0.05 for T1, T2, and T3, respectively, corresponding to trials in which unstable or aborted recoveries associated with legs occurred. Failure 2 occurred less frequently, with probabilities of approximately 0.02, 0.00, and 0.01 for T1, T2, and T3, indicating that the scenarios in which the robot did not immediately recovery (the two modules remained decoupled) after the perturbation, were uncommon.

These results demonstrate that the robot can reliably recover from localized vertical perturbations applied to the body. The consistently high recovery rates across all timing conditions indicate that the mechanical architecture and drivetrain can tolerate temporary compression and disturbance. The low occurrence of unstable recoveries further suggests that the system exhibits robust self-stabilizing behavior following external perturbations.

Discussion

The presented robotic platform simplifies leg assembly and replacement by eliminating mechanical fasteners, allowing tool-free detachment and reattachment of limbs. This enhances serviceability and modularity, particularly advantageous for field repair and reconfigurable experimental platforms. The magnetic interface provides passive overload protection: when a leg experiences excessive resistance during collisions or traversal of confined spaces, the magnetic coupling temporarily disengages, limiting torque transmission and preventing drivetrain damage. This mechanism introduces mechanical compliance analogous to the variable stiffness of insect exoskeletons, which enables shock absorption and terrain adaptability without complex suspension systems[11].

An additional aspect worth considering is that the magnetic coupling strategy may provide a functional analogue of biological preflex mechanisms observed in arthropod locomotion. Preflexes arise from the intrinsic mechanical properties of the musculoskeletal system and generate immediate responses to external perturbations without requiring neural processing delays[12,19]. Similarly, the passive compliance and overload-dependent disengagement enabled by the magnetic interfaces allow the robot to mechanically accommodate unexpected terrain interactions, absorb transient impacts, and redistribute loads before corrective action is produced by the control system. From this perspective, the magnetic transmission not only increases robustness but also represents a bioinspired embodiment of decentralized adaptive behavior, paralleling the contribution of intrinsic mechanical properties to stability and resilience in biological locomotion.

Recent research on hexapod robots has explored different strategies for robustness and multimodality[20–22]. Xi et al.[23] achieved fault tolerance through software-level gait re-planning, whereas the present platform targets miniature hardware robustness via a magnetically coupled transmission

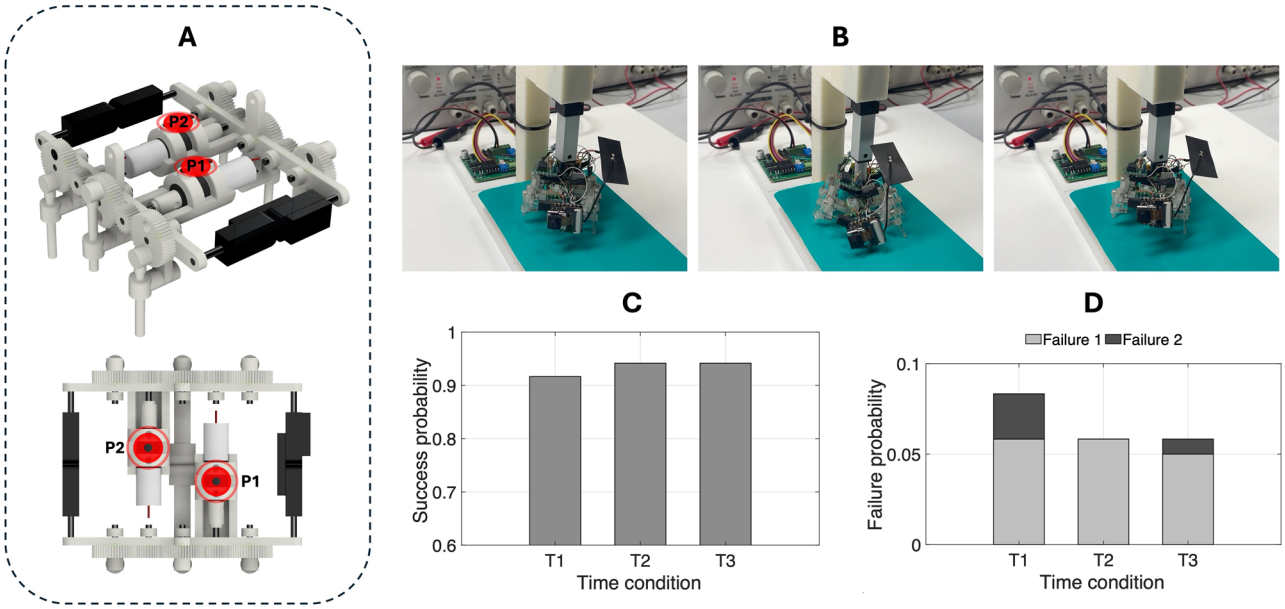


Fig. 6 | Robustness to localized vertical perturbations. A CAD render of the robot with the two perturbation locations highlighted: P1 and P2 (red disks). **B** Representative sequence of a perturbation trial: A motorized linear actuator drives a vertical indenter that presses on the robot body. Three press-hold-release conditions were tested, where the indenter remained in contact with the robot for different durations (T1 = 0.1 s, T2 = 0.5 s, and T3 = 1 s) before being lifted. **C** Recovery success rate for the three perturbation durations. Bars represent the probability that the robot successfully reconfigured after the disturbance. **D** Distribution of observed failure modes across the different perturbation conditions: Failure 1, recovery attempt aborted/unstable due to leg failure, Failure 2, no immediate recovery of the two modules.

that passively sheds overloads. Xu et al.[24] focused on multimodality and mechanism novelty, while our emphasis is a compact locomotor mode with experimentally quantified damage tolerance, controllability, and energetic performance. Advances in MEMS-compatible fabrication support miniaturization while preserving stiffness[25]. Building on this, our design focused on field-deployable simplicity, rapid magnetic assembly, tool-free leg replacement, and fully onboard control, emphasizing repeatable performance under disturbances. A different design philosophy can be observed in RHex-inspired platforms[26–28], where robustness and terrain adaptability are primarily achieved through compliant leg mechanics and distributed actuation. In these systems, each leg is independently actuated, allowing the robot to negotiate challenging terrain through local mechanical interactions and gait dynamics. In contrast, the present platform embeds robustness directly within the drivetrain architecture. Rather than increasing the number of actuators or relying on leg compliance, our design employs multifunctional magnetic couplings that provide torque transmission, passive overload protection, shock tolerance, and proprioceptive sensing, enabling coordinated locomotion with only two actuators and a substantially simplified mechanical architecture.

Magnetic coupling has also been explored in modular legged robots such as Snapbot[29] and its improved version Snapbot V2[30]. In these systems, magnets primarily serve as detachable interfaces that enable rapid attachment and reconfiguration of modular legs, allowing the robot to adapt its locomotion depending on the number and arrangement of limbs. However, locomotion in Snapbot platforms relies on multiple actuators distributed across the legs, with each module containing its own motors and control elements. In contrast, the present platform integrates magnetic coupling directly within the drivetrain architecture and operates with a minimal actuation strategy in which two motors drive synchronized leg modules. In this design, magnets simultaneously transmit torque, provide passive overload protection through controlled slip, and support contactless sensing via Hall effect sensors. Moreover, the overall dimensions and scale of Snapbot-type platforms are not directly comparable to those of the present robot, which is conceived as a compact and lightweight system specifically designed to combine robustness, impact tolerance, and autonomous recovery from disturbances. As a result, while Snapbot emphasizes morphological reconfigurability and actuator-rich locomotion control, our approach prioritizes mechanical simplicity, reduced actuation complexity, and intrinsic resilience at small scale through multifunctional magnetic transmission, passive shock tolerance, and phase-based proprioceptive control.

Beyond the mechanical design, the proposed control strategy also distinguishes the present system from previous work. Coelho et al.[31] regulated body posture based on inferred terrain slope in simulation, whereas our approach controls inter-side phase at the transmission level and validates hardware performance under real contact events, demonstrating centimeter-scale robustness. Ju et al.[32] optimized load-bearing architectures for payload versatility. Our design minimizes complexity while retaining predictable differential steering and low energetic cost. Xiao et al. [33] performed offline co-optimization via Simscape and genetic algorithms. Herin, a closed-loop, phase-based controller operates entirely onboard, augmented by a magnetic micro-clutch providing a physical safety layer.

Other insect-inspired robots have been also developed in previous research, whose locomotion is based on jumping mechanisms, leveraging elastic energy for terrain-independent locomotion[34–36]. However, while burst locomotion extends mobility, our work focused on continuous walking with hardware-integrated compliance and phase control.

Key advantages of the proposed architecture include: (1) passive robustness, with magnetic couplings providing overload protection and automatic re-engagement following disturbances; (2) integrated contactless magnetic sensing using transmission magnets for phase reconstruction; (3) a simple control framework based on phase regulation between the two drive modules, enabling coordinated locomotion and steering maneuvers; and (4) a modular architecture that facilitates rapid assembly, maintenance, and leg replacement. Together, these features promote resilient locomotion while maintaining low mechanical and control complexity.

Compared to traditional elastic elements such as springs, magnetic couplings provide a form of compliance that can simultaneously transmit torque and act as a passive safety mechanism. This allows the drivetrain to

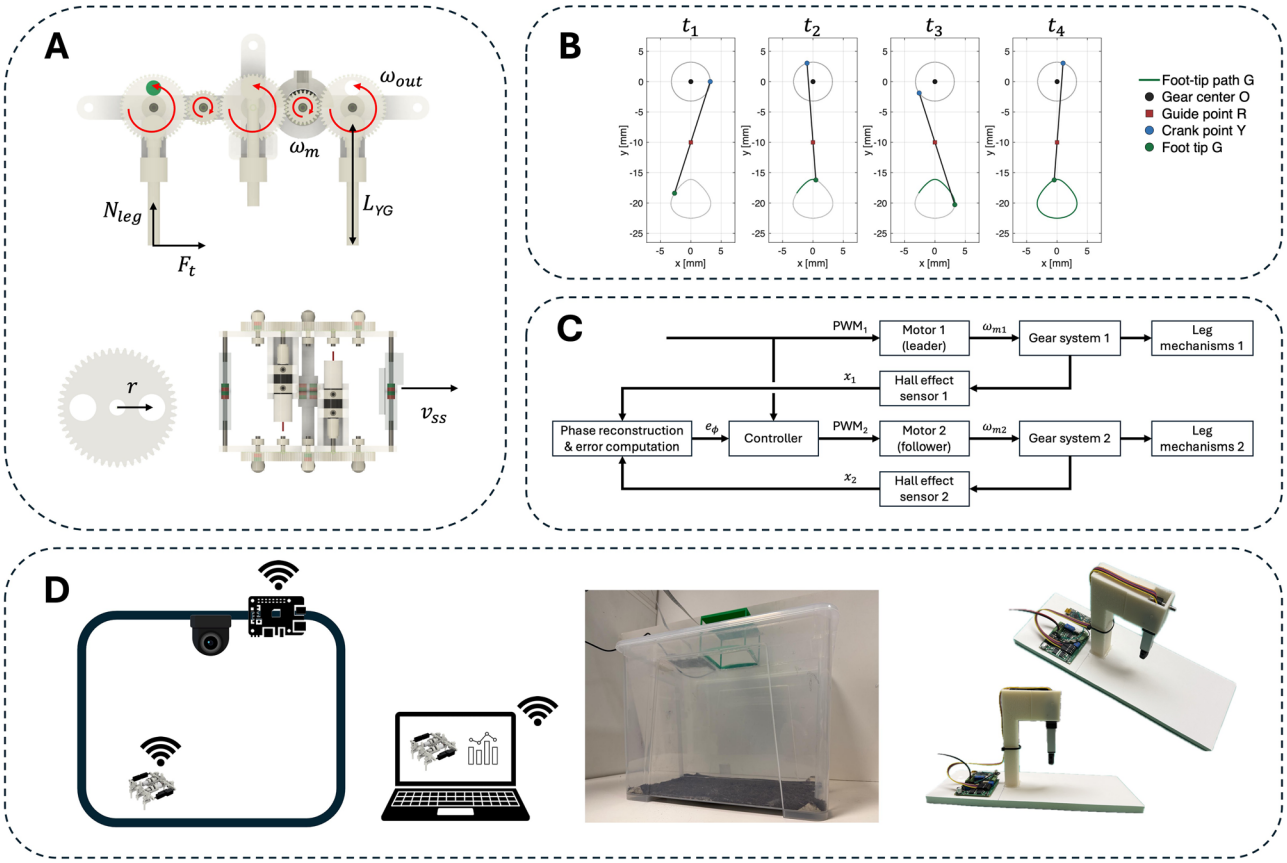


Fig. 7 | Mechanism modeling, control architecture, and experimental setup. **A** Representation of the locomotion mechanism. Motor rotation ω_m is transmitted through a gear reduction stage, producing an output angular velocity ω_{out} that drives the leg mechanism via a crank of radius r. The resulting foot-ground interaction is represented by the tangential and normal forces (F_t and N_{leg}), which generate forward propulsion. **B** Representative configurations of the leg mechanism at different instants during a locomotion cycle (t_1-t_4). The crank point Y rotates around the gear center O, while the constrained leg segment produces the foot-tip trajectory through the passive guide point R. **C** Phase-based leader-follower control architecture. One drive module operates as the leader and is driven at a baseline pulse-width modulation (PWM) duty cycle, while the follower module is regulated using phase feedback reconstructed from two Hall effect sensors to maintain the desired phase relationship between the two sides. **D** Experimental setup. Wireless communication enables real-time monitoring and data acquisition during locomotion experiments. The central image shows the arena used for locomotion trials, while the right images illustrate the actuator-based perturbation apparatus employed to evaluate robustness against external disturbances.

disengage temporarily under excessive loads and automatically re-engage once the disturbance is removed, reducing the risk of mechanical damage. In addition, magnetic interfaces tolerate small misalignments and simplify assembly compared to preloaded spring mechanisms. However, magnetic compliance is inherently limited by the achievable magnetic torque and offers less direct tunability of stiffness than conventional springs, which can store and release elastic energy more efficiently. As a result, magnetic coupling represents a trade-off that favors simplicity, modularity, and damage tolerance over precise stiffness control.

Two magnetic subsystems are central. First, contactless magnet-Hall sensing provides robust feedback for phase control. Second, a passive magnetic micro-clutch slips under excessive torque, preventing motor stall and gear damage, and re-engages automatically. Together, these elements transform magnets into functional components enhancing resistance to impact, misalignment, and jamming.

Quantitative experiments validate the proposed architecture and demonstrate its ability to achieve efficient and controllable locomotion despite the reduced actuation complexity. Straight-line locomotion experiments revealed a monotonic relationship between frequency and forward speed, with locomotion efficiency improving at higher frequencies as reflected by the progressive reduction in both energy per unit distance and Cost of Transport. Additional experiments on inclined terrain confirmed the robustness of the locomotion strategy. Although increasing slope reduced effective forward progression and increased energetic expenditure, stable locomotion was maintained across all tested inclinations.

Maneuverability experiments further demonstrated the versatility of the platform. Differential steering enabled modulation of trajectory curvature, producing predictable variations in both angular speed and turning radius. Spin-in-place provided an additional turning modality, allowing rapid reorientation around the body center while requiring only modest increases in power consumption across the explored operating range. Together, these results demonstrate that a wide range of turning behaviors can be achieved through simple modulation of the drive-module actuation.

Experiments on heterogeneous substrates further highlighted the influence of terrain properties on locomotion performance. While stable locomotion was maintained across all tested conditions, substrate compliance significantly affected both energetic efficiency and power consumption, with grass yielding the lowest transport cost and granular perlite producing the highest energetic demand. Robustness experiments with controlled vertical perturbations revealed a high probability of autonomous recovery (91–95% of trials across different perturbation conditions). Together, these results indicate that integrating passive compliance and overload protection directly within the drivetrain can provide reliable locomotion, maneuverability, and disturbance tolerance in a compact legged robotic platform.

The periodic body motions observed during locomotion are consistent with behaviors reported in biological hexapods, where interlimb coordination, load redistribution, and body-terrain interactions naturally generate oscillatory body dynamics during walking[37–39]. Such dynamics can contribute to adaptive load sharing and robust terrain interaction in systems that rely on compliant body-leg coupling.

High-performance insect-scale platforms such as the Harvard Ambulatory Microrobot (HAMR-F) achieve significantly higher speeds through complex multi-actuator piezoelectric architectures and compliant flexure transmissions[40]. In contrast, INSECTRON adopts a simpler mechanical strategy in which two DC micromotors drive multiple legs through a gear transmission combined with magnetic coupling interfaces. While the resulting locomotion speed is lower than that achieved by high-frequency microrobotic systems, it prioritizes mechanical simplicity and robustness over maximum dynamic performance. From an energetic perspective, the measured CoT falls within the same order of magnitude reported for highly optimized insect-scale robots. Another example is BHMbot, which achieve extremely high running speeds through specialized bouncing locomotion mechanisms[41]. Also compared to this latter case, CoT remains in the same order of magnitude and is comparable. Our proposed design emphasizes robustness, modularity, maneuverability, and passive protection: the magnetic couplings act as micro-clutches that allow automatic disengagement under overload conditions, protecting the drivetrain from impacts or leg entanglement without requiring additional sensing or control. Together, these results suggest that embedding passive compliance and overload protection directly within the drivetrain can provide an effective alternative strategy for achieving reliable locomotion in compact legged robots while maintaining competitive energetic efficiency.

The architecture reduces part count, relaxes alignment tolerances, and simplifies assembly, enabling rapid prototyping and field deployment. Fully integrated onboard electronics, power, sensing, and control allow untethered operation and independent leg-module modulation, minimizing system complexity at the centimeter scale. Trade-offs include tuning magnetic coupling to balance torque transfer and safe slip, with opportunities for torque-proxy sensing, terrain-adaptive feet, and low-power state estimation to extend performance. Scaling studies could guide adaptation to different size regimes.

Phase-based proprioceptive control maintains the desired anti-phase relationship between the two drive modules. This strategy is particularly compatible with the proposed magnetic transmission, as temporary amplitude variations or minor slips do not necessarily compromise phase coordination. As a result, coordinated locomotion can be achieved with limited sensing, low computational requirements, and a simple onboard implementation. Similar control approaches have been widely employed in biologically inspired locomotion systems[42–45].

This work provides a practical alternative to rigid pinned joints in small-scale legged robots, offering a pathway toward robust, manufacturable, and easily serviced miniature mobile robots. Overall, this robotic platform demonstrates that combining magnet-enabled mechanical architecture with onboard sensing and phase-based control produces a miniature hexapod that is damage-tolerant, energetically efficient, and controllable. Its resilience, modularity, and simplicity make it suitable for field deployment in industrial inspection, search-and-rescue, environmental monitoring, swarm robotics, and animal-robot interaction systems[46], bridging laboratory assays and in-situ observations.

Methods

Mechanism and modeling

Locomotion is generated by two magnetically coupled, identical drive modules, with one rotated by 180° relative to the other, each driven by a DC micromotor. The only structural difference lies in one of the magnetic clutches, which was slightly modified to accommodate the onboard electronics. Motor rotation is transmitted through a spur-gear transmission and converted into oscillatory leg motion through a magnetically coupled crank-driven leg mechanism. Within each drive module, three legs are mechanically synchronized to generate a repeatable stance-swing gait (see Fig. 7A).

The gear train distributes motion and torque across the synchronized leg mechanisms. The first reduction stage consists of a motor pinion with z_s teeth engaging a larger gear with $z_b = 2z_s$, resulting in a transmission ratio:

$$i_1 = \frac{z_b}{z_s} = 2 \tag{1}$$

For a transmission composed of m gear stages, the total transmission ratio G_t is given by:

$$G_t = \prod_{k=1}^{m} i_k \tag{2}$$

where i_k denotes the transmission ratio associated with the k-th gear stage. The resulting output angular velocity ω_{out} and output torque τ_{out} are therefore:

$$\omega_{out} = \frac{\omega_m}{G_t} \tag{3}$$

$$\tau_{out} = \eta_{tot}\, G_t\, \tau_m \tag{4}$$

where ω_m and τ_m represent the motor angular velocity and torque, respectively, and η_{tot} is the total transmission efficiency. The total efficiency is modeled as:

$$\eta_{tot} = \prod_{k=1}^{m} \eta_k \tag{5}$$

where η_k represents the efficiency associated with the k-th gear stage.

In the implemented transmission, the first gear stage provides a 2:1 reduction ratio, reducing angular velocity while increasing the transmitted torque. The output gears drive the leg mechanisms through magnetically coupled attachment points positioned at an offset radius r from the gear rotation center.

The magnetic coupling is based on cylindrical NdFeB permanent magnets (grade N50, diameter D = 2.5 mm, height h = 2.5 mm) with axial magnetization. According to the manufacturer specifications, each magnet provides a nominal holding force of 4.32 N and a remanent magnetic flux density of 1.40 T.

The magnetic attachment point drives the leg through a passive hinged guide, allowing combined rotational and sliding motion during the gait cycle. This configuration converts the rotational motion of the gear into an oscillatory foot trajectory while maintaining passive mechanical compliance.

During operation, pairs of facing magnets generate an attractive normal force that enables tangential force transmission between the rotating gear and the guided leg structure. The maximum transmissible torque before disengagement can be approximated as:

$$\tau_{slip} = F_{shear} r \tag{6}$$

where F_{shear} is the maximum transmissible tangential force. The shear force can be approximated as:

$$F_{shear} = \mu_s n_p F_n \tag{7}$$

where μ_s is an effective shear factor accounting for the relationship between magnetic holding force and tangential load capacity, including magnetic field distribution, alignment, interface geometry, air gap, and local contact conditions, n_p is the number of effective magnet pairs, and F_n is the magnetic holding force generated by the facing magnets. Reducing the air gap or

increasing the magnet dimensions increases the magnetic normal force and consequently the maximum transmissible torque of the coupling.

The selected magnet dimensions and magnetic grade provide a compromise between reliable torque transmission during nominal locomotion and passive disengagement under overload conditions. Larger magnets or smaller air gaps increase the magnetic normal force and consequently the maximum transmissible torque, while smaller magnets or larger clearances promote earlier disengagement of the coupling. In the implemented design, NdFeB N50 magnets were selected to ensure stable force transmission during regular gait operation while maintaining passive protection against impacts, terrain obstacles, and leg jamming.

Considering the nominal magnetic holding force reported by the manufacturer ($F_n = 4.32$ N) and the radial distance of the magnetic attachment point from the gear rotation center ($r = 3.2$ mm), the slip torque can be estimated using Eqs. (6) and (7). Assuming an effective shear factor in the range $\mu_s = 0.1$-0.2, the resulting slip torque is approximately 0.001-0.003 Nm per effective magnet pair. If the transmitted torque exceeds τ_{slip}, the magnetic coupling disengages and the leg temporarily decouples from the drivetrain. This mechanism prevents motor stalling and protects the gear train from excessive loads. Once the disturbance is removed, magnetic attraction automatically re-engages the coupling without requiring active control. The passive magnetic disengagement also reduces impulsive load transmission to the drivetrain, improving tolerance to terrain irregularities and reducing long-term mechanical stress accumulation during repetitive locomotion cycles.

If the magnetic coupling remains engaged (i.e., no slip occurs), the angular position of the magnetic attachment point follows the output gear rotation (see Fig. 7B). The crank phase is therefore obtained from the output angular velocity as:

$$\phi(t) = \int \omega_{out}(t)\, dt \tag{8}$$

where ω_{out} is the angular velocity of the output gear.

The magnetic attachment point Y rotates around the gear center O with radius r, such that:

$$Y = \begin{bmatrix} r\cos\phi \\ r\sin\phi \end{bmatrix} \tag{9}$$

The leg is modeled as a rigid segment of constant length L_{YG} constrained through a passive hinged guide point R. The resulting foot-tip position G can therefore be expressed as:

$$G = Y + L_{YG}\frac{R - Y}{||R - Y||} \tag{10}$$

This kinematic constraint converts the rotational motion of the gear into a periodic foot trajectory generating alternating stance and swing phases during locomotion. The resulting constrained leg kinematics produce both longitudinal propulsion and vertical lifting of the foot throughout the gait cycle. The local transmission between rotational motion and foot displacement can be described through the kinematic Jacobian of the leg mechanism:

$$J(\phi) = \frac{\partial G}{\partial \phi} \tag{11}$$

Assuming an effective horizontal foot excursion Δx_f, the nominal stride length can be approximated as:

$$L_s = \Delta x_f \tag{12}$$

and the forward velocity scales approximately with stepping frequency f_s:

$$v \propto f_s L_s \tag{13}$$

The propulsive force generated during stance is limited by the transmissible torque of the magnetic coupling and by the frictional interaction between the foot and the substrate. Assuming N_s effective supporting legs during stance, the normal load supported by each leg can be approximated as:

$$N_{leg} = \frac{mg}{N_s} \tag{14}$$

where m is the robot mass, and g is gravitational acceleration.

Ground interaction is modeled through a Coulomb friction constraint:

$$\left|F_t(\phi)\right| \le \mu_g N_{leg} \tag{15}$$

where μ_g is the effective friction coefficient between the foot and the substrate. If the tangential force exceeds this limit, foot slip occurs and propulsion efficiency decreases.

Assuming that locomotion can be approximated by the balance between the average propulsive forces generated by the left and right drive modules and the dissipative forces acting on the robot, the forward dynamics can be expressed as:

$$m\dot{v} = \bar{F}_L + \bar{F}_R - c_v v \tag{16}$$

where $\bar{F}_L$ and $\bar{F}_R$ are the mean propulsive forces generated by the left and right drive modules, respectively, and c_v is an equivalent viscous coefficient accounting for energy dissipation arising from foot-ground interactions, impacts, and other locomotion losses. Under steady-state conditions, the corresponding forward velocity becomes:

$$v_{ss} = \frac{\bar{F}_L + \bar{F}_R}{c_v} \tag{17}$$

The torque available at the gearbox output ultimately depends on the operating point of the DC micromotor. Under steady-state conditions, the motor exhibits the linear torque-speed characteristic:

$$\tau_m(\omega_m) = \tau_{stall}\left(1 - \frac{\omega_m}{\omega_{nl}}\right) \tag{18}$$

where τ_{stall} and ω_{nl} denote the stall torque and no-load speed of the motor, respectively. Through the gearbox reduction, this characteristic determines the torque available at the output shaft and consequently the force that can be transmitted to the leg mechanism.

Assuming that each drive module generates a forward velocity proportional to its stepping frequency and effective stride length, the equivalent left and right module velocities can be approximated as:

$$v_L \propto f_L L_s \tag{19}$$

$$v_R \propto f_R L_s \tag{20}$$

where f_L and f_R are the stepping frequencies of the left and right modules, respectively.

Using a differential-drive approximation with effective track width W_e, the body linear and angular velocities become:

$$v = \frac{v_L + v_R}{2} \tag{21}$$

$$\omega = \frac{v_L - v_R}{W_e} \tag{22}$$

The corresponding turning radius is therefore:

$$R_t = \frac{v}{\omega} = \frac{W_e}{2}\frac{v_L + v_R}{v_L - v_R} \tag{23}$$

This simplified analytical model provides an order-of-magnitude link between drivetrain torque, ground interaction, and the observed locomotion speed and turning performance. A magnet-Hall pair on each side provides an indirect measurement of the crank phase ϕ. Instantaneous phase is reconstructed from the normalized Hall effect sensor signal and made continuous over time. The controller regulates the phase error relative to the 180° anti-phase target. This keeps the two modules in persistent anti-phase while preserving the gear-locked in-phase coordination of the three legs per side.

Design and fabrication

The proposed platform is a miniaturized hexapod robot with an overall body length of 8.7 cm and a total mass of 33.9 g. Mechanism and chassis were CAD-designed. Load-bearing parts (gears, carriers, hubs) were additively manufactured on a ProJet MJP 3600 in VisiJet® M3 Crystal. Auxiliary components were printed in PLA on a Bambu Lab P1P. Steel pins (Ø 1.5 mm, L 8-10 mm) were employed as axles where required. Permanent magnets (NdFeB, N50, 2.5×2.5 mm) with a nominal holding force of 4.32 N were used. The control electronics comprise a Seeed Studio XIAO ESP32-S3 and a DRV8833 dual H-bridge to drive the two DC motors. Two 49E bipolar Hall effect sensors were employed. Each sensing unit exploits the transmission magnet together with an additional permanent magnet mounted 180° apart. The two magnets present opposite magnetic poles to the Hall effect sensor during rotation, generating the periodic magnetic signal used for phase reconstruction. Tests were performed from a single-cell Li-ion supply (4.2-3.6 V). Motor commands are issued as pulse-width modulation (PWM) duty cycles. Electrical current consumption was measured through a shunt resistor placed on the system ground and amplified using an operational amplifier to obtain a measurable voltage signal. This signal was acquired by the onboard microcontroller and transmitted wirelessly via Wi-Fi for logging and offline analysis. This hardware architecture also provides passive overload protection while simplifying maintenance and assembly. Magnetic couplings replace conventional pinned joints and mechanical fasteners, and the attractive magnetic forces naturally self-align the coupled components. As a result, the system tolerates small positional or angular misalignments that would otherwise cause binding or excessive wear in rigid pin-based joints, eliminating the need for precise mechanical alignment during assembly or replacement of the legs.

Control strategy

A phase-based controller was implemented to maintain in persistent anti-phase (180° phase offset) the two drive modules (see Fig. 7C). The controller was executed at a nominal frequency of 100 Hz. At each control cycle ($T_s = 10$), two Hall effect sensor signals $x_1(k), x_2(k) \in [-1, 1]$ were acquired, normalized, filtered using a moving average filter with a window size $N_w = 5$, and expressed in a common phase convention. For each signal, an instantaneous wrapped phase was reconstructed using the inverse sine function. The sign of the signal derivative was then used to resolve the quadrant ambiguity:

$$\phi_{0,i}(k) = \arcsin\big(x_i(k)\big) \tag{24}$$

$$\phi_i^*(k) = \begin{cases} \phi_{0,i}(k), & \dot{x} \geq 0 \\ \pi - \phi_{0,i}(k), & \dot{x} < 0 \end{cases} \tag{25}$$

with

$$\dot{x}_i(k) = \frac{x_i(k) - x_i(k-1)}{T_s} \tag{26}$$

The wrapped phase was then unwrapped recursively to obtain a continuous phase:

$$\phi_i(k) = \phi_i(k-1) + wrap_\pi\big(\phi_i^*(k) - \mathrm{mod}\big(\phi_i(k-1), 2\pi\big)\big) \tag{27}$$

where $\mathrm{wrap}_\pi(\cdot) \in (-\pi, \pi]$ prevents discontinuities at cycle transitions.

One module was selected as the leader, driven at the baseline PWM duty cycle, while the other module acted as the follower. The phase error was computed as the wrapped difference between the follower phase and the leader phase relative to the desired anti-phase condition:

$$e_\phi(k) = wrap_\pi\big(\big(\phi_2(k) - \phi_1(k)\big) - \pi\big) \tag{28}$$

A proportional-derivative (PD) controller was employed to compute the PWM command (8-bit microcontroller representation of the PWM duty cycle) applied to the follower module according to:

$$u(k) = u_0 + k_p e_\phi(k) + k_d \dot{e}_\phi(k) \tag{29}$$

where u_0 is the baseline PWM command. In the implemented controller, $k_p = 100$ and $k_d = 10$. The resulting output was saturated to the admissible range [0,255].

By directly regulating the phase error, the controller maintains the desired anti-phase coordination between the two drive modules, while compensating for frequency mismatches between the two drive modules.

Maneuverability was evaluated using two strategies:

- Differential turning. The two drive modules were actuated at different frequencies. According to the differential-drive approximation introduced in Eqs. (21)-(23), the resulting angular speed and turning radius are determined by the frequency difference between the two sides. Experimentally, the steering behavior was characterized as a function of the imposed frequency difference $|\Delta f| = |f_L - f_R|$:

$$|\omega| = k_\omega |\Delta f| \tag{30}$$

$$R_t = \frac{v}{|\omega|} \tag{31}$$

  where k_ω denotes the proportionality coefficient. Increasing the frequency difference increases the angular speed while reducing the turning radius, enabling predictable control of trajectory curvature.

- Spin-in-place. In this mode, the two drive modules were actuated at the same frequency but in opposite directions. The phase-based controller continued to regulate the relative phase of the two modules, maintaining the desired anti-phase relationship. Under these conditions, the translational velocity components approximately cancel, producing a predominantly rotational motion about the body center. The resulting angular speed was experimentally characterized as a function of the common drive frequency.

Experimental setup

Experiments were conducted in a boxed arena lined with 1.3 cm grid paper to provide spatial calibration for motion tracking (see Fig. 7D). Videos were recorded from above using a Raspberry Pi 4 equipped with a Raspberry Pi Camera Module 3 (1080p, 30 fps), with the optical axis normal to the ground plane. The grid pattern allowed accurate reconstruction of the robot trajectory and displacement during locomotion trials.

The robot operated fully untethered during all experiments. An onboard microcontroller continuously transmitted sensor readings, motor commands, and current measurements to a remote computer via Wi-Fi. The robot was connected to the local network and streamed telemetry in real time throughout the experiments, enabling synchronized data logging without any wired connection to the robot.

In addition, the arena platform was adjustable to introduce controlled inclinations, and tests were conducted at slopes of 3° and 5° to evaluate the effect of terrain gradients on locomotion performance. Locomotion experiments were performed also on different substrates to evaluate the robustness of the mechanism under varying contact conditions. For the different substrates we considered:

- A commercial cultivation soil substrate was used to reproduce a soft, organic terrain. The material consists of peat-based soil amended with composted organic matter and mineral fertilizer (NPK), characterized by high porosity (92%) and low bulk density (100 kg/m^3), providing a compliant and deformable ground condition for locomotion tests.
- Quartz sand (EN 13139, category 0/1) with particle size ranging from 0.3 to 0.6 mm was used to reproduce a loose granular substrate. The material is characterized by low moisture content (< 0.5%) and uniform grain size, providing a controlled and repeatable sandy terrain for locomotion experiments.
- Expanded perlite (particle size 2–6 mm) was used to reproduce a coarse granular substrate. Perlite is a lightweight volcanic glass expanded through thermal processing, resulting in highly porous particles with low bulk density and limited inter-particle cohesion. The relatively large particle size and low packing density provide a deformable and unstable terrain, allowing the evaluation of locomotion performance under conditions characterized by reduced support and increased energy dissipation during foot-ground interaction.
- Natural grass terrain was used to assess locomotion performance under realistic outdoor conditions. Experiments were conducted directly in the field on a vegetated surface composed of grass and underlying natural soil. This environment introduces spatial variability in ground stiffness, surface roughness, and vegetation density, providing a representative scenario for evaluating the robustness of the robot in unstructured real-world environments.

For perturbation experiments, external vertical loads were applied using a motorized linear actuation system. A vertically oriented linear actuator drove a rigid indenter that contacted the robot body at two different dorsal locations (P1 and P2, see Fig. 6), allowing evaluation of the drive-train's overload protection and mechanical robustness. The actuator displacement and velocity were controlled through a motor driver and microcontroller, enabling repeatable press-release profiles. Three press-hold-release conditions were tested, denoted as T1-T3, which differed in the duration for which the indenter remained in contact with the robot before being lifted. Specifically, the indenter was held stationary on the robot body for 0.1 s, 0.5 s, and 1 s, respectively, before the release phase. This allowed us to evaluate the system response under different perturbation persistence conditions.

Performance assessment

Locomotion and energetics were quantified from time-stamped pose data and synchronous electrical measurements. Forward speed was obtained from planar trajectories $x(t)$, $y(t)$, and speed was computed as:

$$v(t) = \frac{ds}{dt} \tag{32}$$

For each trial, the frequency of each drive module was estimated from the corresponding Hall effect sensor signal and assigned as the drive frequency of the left and right sides (f_L,f_R). The inter-side frequency difference was then computed as $\Delta f = |f_L - f_R|$.

Electrical power was computed as

$$P = V \cdot \bar{I} \tag{33}$$

where V is the motor supply voltage and $\bar{I}$ is the mean current measured over the duration of the experiment for the considered test condition. Energy per meter was computed as:

$$E_m = \frac{P}{v}[\mathrm{J/m}] \tag{34}$$

Cost of Transport (CoT) was computed as:

$$\mathrm{CoT} = \frac{P}{mgv} = \frac{E_\mathrm{m}}{mg} \tag{35}$$

with robot mass $m = 0.0339$ kg and $g = 9.81$ m/s^2.

Statistical reporting: values are mean ± SD across repeats.

Data availability

All data supporting the findings of this study are available within the paper and its Supplementary Information.

Received: 8 October 2025; Accepted: 27 June 2026;
Published online: 05 November 2026

References

1. Sharma, B. Robotic dog for navigation of a rehabilitation wheelchair robot in a highly constrained environment. *PLoS One* **19**, e0310024 (2024).
2. Antony, B., Anand, S., & Satyarthi, M. K. Biomimetic Bipedal Locomotion: Avian-Inspired Dynamics and Simulation Analysis. In *International Conference on Mechanical and Energy Technologies* (pp. 477-483). (Springer Nature Singapore. 2023).
3. Nguyen, C. T. et al. Development of an insect-inspired hexapod robot actuated by soft actuators. *J. Mechanisms Robot.* **10**, 061016 (2018).
4. Dickinson, M. H. et al. How animals move: an integrative view. *Science* **288**, 100–106 (2000).
5. Schaeffer, P. J. & Lindstedt, S. L. How animals move: comparative lessons on animal locomotion. *Compr. Physiol.* **3**, 289–314 (2013).
6. Ding, X., Wang, Z., Rovetta, A. & Zhu, J. M. Locomotion analysis of hexapod robot. *Climbing Walk. Robots* **30**, 291–310 (2010).
7. Shah, D. et al. A comprehensive review of hexapod robots: advancements, challenges, and applications. *Nirma Univ. J. Eng. Technol.* **2**, 12–19 (2024).
8. Liang, R. et al. Research on the design and application of bionic hexapod robot system. *J. Braz. Soc. Mech. Sci. Eng.* **47**, 375 (2025).
9. Machado, J. T., & Silva, M. F. An overview of legged robots. In *International Symposium on Mathematical Methods in Engineering* (Vol. 48, No. 2.3). (MME Press, 2006).
10. Wootton, R. J. Invertebrate paraxial locomotory appendages: design, deformation and control. *J. Exp. Biol.* **202**, 3333–3345 (1999).
11. Jayaram, K. & Full, R. J. Cockroaches traverse crevices, crawl rapidly in confined spaces, and inspire a soft, legged robot. *Proc. Natl. Acad. Sci.* **113**, E950–E957 (2016).
12. Brown, I. E., & Loeb, G. E. A reductionist approach to creating and using neuromusculoskeletal models. In *Biomechanics and Neural Control of Posture and Movement* (pp. 148-163). (Springer New York, 2000).
13. Sun, H., Hu, K., Si, Q., Lan, Q., & Yuan, S. Review of fault modes and failure diagnosis methods for magnetic-driving pump. *Structural Health Monitoring*, 14759217251316621. https://doi.org/10.1177/14759217251316621 (2025).
14. Li, Z., Yuan, Z., Li, X., Wang, M., & Zhu, G. Research on dynamic coupling characteristics of magnetic fluid and gas medium interface in sealing devices. *Phys. Fluids*, 35. https://doi.org/10.1063/5.0149545 (2023).

15. Stefanini, C. et al. A novel autonomous, bioinspired swimming robot developed by neuroscientists and bioengineers. *Bioinspiration Biomim.* **7**, 025001 (2012).
16. Manduca, G., et al. A Novel Underwater Robot with Carangiform Locomotion Achieved via Single Degree of Actuation and Magnetically Transmitted Traveling Wave. In *2025 IEEE International Conference on Robotics and Automation (ICRA)* (pp. 14665-14670). IEEE. (2025, May).
17. Suvorov, V. A. et al. Mathematical model and experimental study of a magnet coupling with a stop. *SN Appl. Sci.* **4**, 286 (2022).
18. Lukočius, R. et al. An analysis of axial magnetic coupling force and torque dependencies on its structure parameters using a 3D FEM. *Appl. Sci.* **12**, 6546 (2022).
19. Daley, M. A., Voloshina, A. & Biewener, A. A. The role of intrinsic muscle mechanics in the neuromuscular control of stable running in the guinea fowl. *J. Physiol.* **587**, 2693–2707 (2009).
20. Song, X., Zhang, X., Meng, X., Chen, C. & Huang, D. Gait optimization of step climbing for a hexapod robot. *J. Field Robot.* **39**, 55–68 (2022).
21. Wang, C. et al. Review of bionic crawling micro-robots. *J. Intell. Robotic Syst.* **105**, 56 (2022).
22. Zhang, G. et al. Q-Whex: A simple and highly mobile quasi-wheeled hexapod robot. *J. Field Robot.* **40**, 1444–1459 (2023).
23. Xi, Q., Chen, Z., Yin, K., Liu, X. & Gao, F. Fault-tolerant gait for Hexapod Robots with partial active joints locked. *Mechanism Mach. Theory* **205**, 105895 (2025).
24. Xu, K. et al. Design and multimodal locomotion plan of a hexapod robot with improved knee joints. *J. Field Robot.* **41**, 1279–1296 (2024).
25. Sugimoto, K. & Nagasawa, S. Micro-hexapod robot with an origami-like SU-8-coated rigid frame. *Robotica* **42**, 1614–1627 (2024).
26. Saranli, U., Buehler, M. & Koditschek, D. E. RHex: A simple and highly mobile hexapod robot. *Int. J. Robot. Res.* **20**, 616–631 (2001).
27. Sun, C. et al. RHex-T3: A transformable hexapod robot with ladder climbing function. *IEEE/ASME Trans. Mechatron.* **28**, 1939–1947 (2023).
28. Shao, Q. et al. Unearthing the history with A-RHex: Leveraging articulated hexapod robots for archeological pre-exploration. *J. Field Robot.* **42**, 206–218 (2025).
29. Kim, J., Alspach, A., & Yamane, K. Snapbot: A reconfigurable legged robot. In *2017 IEEE/RSJ International Conference on Intelligent Robots and Systems (IROS)* (pp. 5861-5867). IEEE. (2017, September).
30. Gim, K. G., & Kim, J. Snapbot v2: a reconfigurable legged robot with a camera for self configuration recognition. In *2020 IEEE/RSJ International Conference on Intelligent Robots and Systems (IROS)* (pp. 4026-4031). (IEEE, 2020).
31. Coelho, J., Dias, B., Lopes, G., Ribeiro, F. & Flores, P. Development and implementation of a new approach for posture control of a hexapod robot to walk in irregular terrains. *Robotica* **42**, 792–816 (2024).
32. Ju, Z., Wu, R., Guo, D. & Xu, Y. Development of a Load-Bearing, Terrain-Adaptive Hexapod Robot With Chebyshev-Linkage Legs. *J. Field Robot.* **42**, 1439–1462 (2025).
33. Xiao, Y., Yin, K., Chen, X., Chen, Z. & Gao, F. Multi-objective optimization design method for the dimensions and control parameters of curling hexapod robot based on application performance. *Mechanism Mach. Theory* **204**, 105831 (2024).
34. Mo, X. et al. Locust-inspired jumping mechanism design and improvement based on takeoff stability. *J. Mechanisms Robot.* **16**, 061013 (2024).
35. Ribak, G. Insect-inspired jumping robots: challenges and solutions to jump stability. *Curr. Opin. Insect Sci.* **42**, 32–38 (2020).
36. Scarfogliero, U., Stefanini, C., & Dario, P. Design and development of the long-jumping" grillo" mini robot. In *Proceedings 2007 IEEE International Conference on Robotics and Automation* (pp. 467-472). IEEE. (2007, April).
37. Dürr, V., Schmitz, J. & Cruse, H. Behaviour-based modelling of hexapod locomotion: linking biology and technical application. *Arthropod Struct. Dev.* **33**, 237–250 (2004).
38. Fukuhara, A., Suda, W., Kano, T., Kobayashi, R. & Ishiguro, A. Adaptive interlimb coordination mechanism for hexapod locomotion based on active load sensing. *Front. Neurorobotics* **16**, 645683 (2022).
39. Wang, Y., Othayoth, R. & Li, C. Cockroaches adjust body and appendages to traverse cluttered large obstacles. *J. Exp. Biol.* **225**, jeb243605 (2022).
40. Goldberg, B. et al. Power and control autonomy for high-speed locomotion with an insect-scale legged robot. *IEEE Robot. Autom. Lett.* **3**, 987–993 (2018).
41. Liu, Z. et al. A wireless controlled robotic insect with ultrafast untethered running speeds. *Nat. Commun.* **15**, 3815 (2024).
42. Bjelonic, M., Kottege, N., & Beckerle, P. Proprioceptive control of an over-actuated hexapod robot in unstructured terrain. In *2016 IEEE/RSJ International Conference on Intelligent Robots and Systems (IROS)* (pp. 2042-2049). https://doi.org/10.1109/IROS.2016.7759321 (2016, October).
43. Eich, M., Grimminger, F., & Kirchner, F. Proprioceptive control of a hybrid legged-wheeled robot. In *2008 IEEE International Conference on Robotics and Biomimetics* (pp. 774-779). https://doi.org/10.1109/ROBIO.2009.4913098 (IEEE, 2009).
44. Manduca, G. et al. A bioinspired control strategy ensures maneuverability and adaptability for dynamic environments in an underactuated robotic fish. *J. Intell. Robotic Syst.* **110**, 69 (2024).
45. Seok, S., Wang, A., Otten, D., & Kim, S. Actuator design for high force proprioceptive control in fast legged locomotion. In *2012 IEEE/RSJ International Conference on Intelligent Robots and Systems* (pp. 1970-1975). https://doi.org/10.1109/IROS.2012.6386252 (IEEE, 2012).
46. Schmickl, T. & Romano, D. Robots and animals teaming up in the wild to tackle ecosystem challenges. *Sci. Robot.* **9**, eado5566 (2024).

Acknowledgements

The authors thank Professor Cesare Stefanini for helpful discussions on the topic. The authors are also grateful to Mr. Godfried Jansen Van Vuuren, Mr. Akshat Wahi, Miss Federica Daga, Mr. Luigifilippo D'Agnolo, and Mr. Nicodemo Funaro for their kind assistance during experiments. This research was carried out in the framework of the EU HORIZON PATHFINDEROPEN Project 'SENSORBEES– Sensorbees are ENhanced Self-ORganizing Bio-hybrids for Ecological and Environmental Surveillance' [101130325], and the Italian Space Agency (ASI) DC-DSR-UVS-2022-375 Project 'pRomoting pEdogenesis througH lunar sOil-terrestriaL organIsms interaction For moon FErtilization – REGOLIFE' [ASI N.: 2024-7-U.0; CUP: J83C24000310005]. Funders had no role in the study design, data collection and analysis, decision to publish, or preparation of the manuscript.

Author contributions

D. R.: conceptualization; methodology; investigation; formal analysis; funding acquisition; project administration; writing review and editing; writing original draft; supervision. G.M.: methodology; investigation; formal analysis; writing review and editing; writing original draft.

Competing interests

The authors declare no competing interests.

Additional information

Supplementary information The online version contains supplementary material available at https://doi.org/10.1038/s44182-026-00106-y.

Correspondence and requests for materials should be addressed to Donato Romano.

Reprints and permissions information is available at http://www.nature.com/reprints

Publisher's note Springer Nature remains neutral with regard to jurisdictional claims in published maps and institutional affiliations.

Open Access This article is licensed under a Creative Commons Attribution-NonCommercial-NoDerivatives 4.0 International License, which permits any non-commercial use, sharing, distribution and reproduction in any medium or format, as long as you give appropriate credit to the original author(s) and the source, provide a link to the Creative Commons licence, and indicate if you modified the licensed material. You do not have permission under this licence to share adapted material derived from this article or parts of it. The images or other third party material in this article are included in the article's Creative Commons licence, unless indicated otherwise in a credit line to the material. If material is not included in the article's Creative Commons licence and your intended use is not permitted by statutory regulation or exceeds the permitted use, you will need to obtain permission directly from the copyright holder. To view a copy of this licence, visit http://creativecommons.org/licenses/by-nc-nd/4.0/.

© The Author(s) 2026